

# Conformational Dynamics of Mechanically Compliant DNA Nanostructures from Coarse-Grained Molecular Dynamics Simulations

Ze Shi,<sup>†</sup> Carlos E. Castro,<sup>‡</sup> and Gaurav Arya<sup>\*,†</sup>

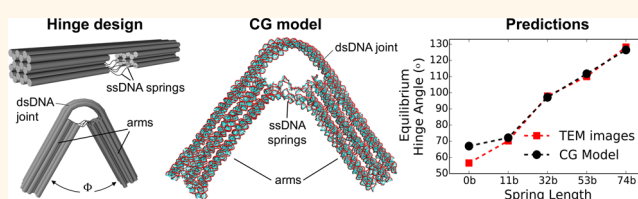
<sup>†</sup>Department of NanoEngineering, University of California, San Diego, La Jolla, California 92093, United States

<sup>‡</sup>Department of Mechanical and Aerospace Engineering, The Ohio State University, Columbus, Ohio 43210, United States

**S** Supporting Information

**ABSTRACT:** Structural DNA nanotechnology, the assembly of rigid 3D structures of complex yet precise geometries, has recently been used to design dynamic, mechanically compliant nanostructures with tunable equilibrium conformations and conformational distributions. Here we use coarse-grained molecular dynamics simulations to provide insights into the conformational dynamics of a set of mechanically compliant DNA nanostructures—DNA hinges that use single-stranded DNA “springs” to tune the equilibrium conformation of a layered double-stranded DNA “joint” connecting two stiff “arms” constructed from DNA helix bundles. The simulations reproduce the experimentally measured equilibrium angles between hinge arms for a range of hinge designs. The hinges are found to be structurally stable, except for some fraying of the open ends of the DNA helices comprising the hinge arms and some loss of base-pairing interactions in the joint regions coinciding with the crossover junctions, especially in hinges designed to exhibit a small bending angle that exhibit large local stresses resulting in strong kinks in their joints. Principal component analysis reveals that while the hinge dynamics are dominated by bending motion, some twisting and sliding of hinge arms relative to each other also exists. Forced deformation of the hinges reveals distinct bending mechanisms for hinges with short, inextensible springs *versus* those with longer, more extensible springs. Lastly, we introduce an approach for rapidly predicting equilibrium hinge angles from individual force-deformation behaviors of its single- and double-stranded DNA components. Taken together, these results demonstrate that coarse-grained modeling is a promising approach for designing, predicting, and studying the dynamics of compliant DNA nanostructures, where conformational fluctuations become important, multiple deformation mechanisms exist, and continuum approaches may not yield accurate properties.

**KEYWORDS:** DNA origami, DNA hinges, molecular dynamics simulations, coarse-grained modeling, dynamic nanostructures, compliant mechanisms, conformational fluctuations



The concept of scaffolded DNA origami<sup>1</sup> has accelerated the progress in DNA nanotechnology by enabling faster and more efficient design of structures with complex geometries. An exquisite array of 2D and 3D nanostructures have been created by DNA origami that include templated nanotubes,<sup>2,3</sup> nanoribbons,<sup>4</sup> nanopores,<sup>5</sup> nanoparticles,<sup>6,7</sup> nanoscale molds<sup>8</sup> and drug delivery vehicles,<sup>9,10</sup> just to name a few. With the advent of computer-aided design tools like caDNAo,<sup>11</sup> Tiamat,<sup>12</sup> CanDo,<sup>13,14</sup> and DAEDALUS,<sup>15</sup> the design and fabrication of such DNA nanostructures is now a relatively fast and well-developed process. Though a majority of structures built *via* DNA origami are mechanically rigid, researchers have begun to create “dynamic structures” that exhibit large-scale thermal fluctuations about a stable conformational state or transitions across multiple stable states, features synonymous with biological molecular motors and enzymes. For instance, by exploiting differences in the mechanical

properties of single-stranded DNA (ssDNA), double-stranded DNA (dsDNA), and bundles of interconnected dsDNA helices, researchers have created a new class of nanostructures such as hinges and pistons whose equilibrium conformational distributions and mechanical compliance is determined by the competition between tension in the ssDNA components and compressive or bending resistance of the dsDNA components.<sup>16–18</sup> These structures can be designed to exhibit specific conformational changes with tunable energy landscape and mechanical stiffness.<sup>17–19</sup>

Much like compliant mechanisms have expanded the functional scope of macroscopic machines, these dynamic structures can be used as the building blocks of next-generation

**Received:** January 11, 2017

**Accepted:** April 19, 2017

**Published:** April 19, 2017

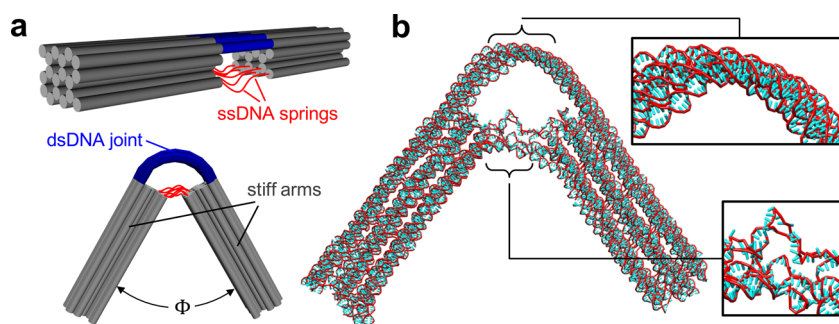


**Figure 1.** Coarse-grained (CG) modeling of DNA origami hinges. (a) Schematic of the hinge illustrating its three main components: a compliant “joint” (blue) composed of  $6 \times 1$  layer of interconnected 84-base long dsDNA helices; a pair of stiff “arms” (gray), each composed of a stacked  $6 \times 3$  bundle of interconnected dsDNA helices arranged in a honeycomb lattice; and six flexible ssDNA “springs” (red). Altering the length of the ssDNA springs from 0 to 74 bases leads to an increase in the hinge angle  $\Phi$  (defined as the angle subtended by two arms) from  $\sim 55^\circ$  to  $\sim 130^\circ$ . (b) CG model of a representative hinge (with 32-base long springs) used for simulating its conformational dynamics; also shown are closeup views of the joint and the springs. The model was rendered using the UCSF Chimera program.<sup>45</sup>

nanodevices and nanomachines with programmed response to physical interactions with the local environment. Critical to this vision is the availability of modeling tools that would allow researchers to predict the molecular-scale conformation, dynamics, structural stability, and mechanical behavior of structural designs. In the past, the nearest-neighbor model of DNA base-pairing<sup>20</sup> has been used to predict the native secondary structure, and the associated free energy, of DNA nanostructures or their motifs.<sup>21,22</sup> To predict 3D tertiary conformations, methods have been developed that impose geometrical restraints on DNA nucleotides which are minimized using relaxation algorithms to yield conformations with minimal mechanical, planar, and torsional strains.<sup>23</sup> Continuum mechanics formulations treating DNA base-pairs as finite elements of an elastic rod, connections between dsDNA helices as rigid crossovers, and ssDNA components as nonlinear springs have also been developed to predict conformations of DNA origami structures designed with typical honeycomb or square lattice cross sections.<sup>13,14</sup> Recent extensions to this approach<sup>24,25</sup> account for lattice-free structures with multiway junctions, topologically closed structures, and Brownian dynamics of the structures. While these continuum-mechanics-based approaches enable rapid predictions of the global conformations of rigid to semiflexible structures, they do not possess the resolution required to capture molecular-scale effects, such as inelastic deformation and partial unzipping of dsDNA components, and conformational flexibility, steric interactions, and secondary-structure formation of ssDNA components. Such effects likely become important in dynamic structures like the DNA hinges discussed earlier that contain long, flexible ssDNA connections and strongly deformed dsDNA components. These approaches are also unable to model structures with complex energy landscapes that exhibit multiple stable conformational states. Lastly, the approaches cannot capture structural “dynamics”, that is, the real-time molecular-scale motions accompanying conformational fluctuations and transitions across states. While these motions are mostly restricted to near-harmonic oscillations in the case of rigid structures, they may become large and lead to more complex, coupled motions in compliant structures.

All-atom models provide an ideal resolution for capturing the conformation and mechanics of the single- and double-stranded components of DNA nanostructures, and molecular dynamics (MD) simulations provide a powerful approach for simulating

their conformational dynamics. Indeed, all-atom MD simulations has increasingly being used to study DNA nanostructures.<sup>25–31</sup> However, many of these structures contain thousands of nucleotides, which equates to simulation systems containing millions of atoms in explicit solvent. Despite rapid advances in computing power, simulating such structures with all-atom models remains highly computationally demanding. To overcome this challenge, a number of coarse-grained (CG) models have been developed that provide simpler representations of DNA while still retaining enough details to reproduce its key properties.<sup>32</sup> *OxDNA*<sup>33</sup> is one such CG model that was recently developed specifically for DNA nanotechnology and reproduces various thermodynamic and conformational properties of ssDNA and dsDNA. This model represents each nucleotide as a rigid body with three interaction sites and accounts for Watson–Crick base pairing, base stacking, excluded volume, and backbone connectivity. *OxDNA* has already been successfully used to study a variety of DNA nanostructures,<sup>34–41</sup> including those built *via* DNA origami.<sup>42–44</sup> However, it remains to be seen if *oxDNA* could predict the dynamical behavior of mechanically compliant DNA nanostructures and if this model could be used to elucidate their conformations, dynamics, and mechanical behavior.

In this study, we investigated the ability of the *oxDNA* model and MD simulations to predict the conformational dynamics of mechanically compliant DNA devices. For our analysis, we chose the set of compliant DNA origami hinges designed, fabricated and studied experimentally by Castro and co-workers.<sup>18</sup> The hinges exhibit an angular bending degree-of-freedom ubiquitous in macroscopic machines, especially in compliant mechanisms, and therefore they are an excellent prototype for dynamic, functionally relevant nanodevices. In particular, the hinges are composed of stiff “arms”, comprised of a bundle of interconnected dsDNA helices, connected by a compliant dsDNA “joint” and flexible ssDNA “springs”, and the angle between the arms could easily be tuned by changing the length of the springs (see Figure 1 and caption). The hinges were extensively characterized, providing a wealth of experimental data for comparison. Our results demonstrate excellent agreement between the predicted hinge angles and those measured experimentally, suggesting that CG modeling and simulations could be an effective predictive tool for designing dynamic DNA nanostructures. We also used the model to elucidate the conformational fluctuations, global dynamics, base-pairing stability, and large-deformation behavior of the

DNA hinges, revealing useful nanoscopic insights into the properties of mechanically compliant DNA devices. Lastly, we demonstrate how macroscopic machine design principles could be coupled with microscopic behavior of individual DNA components obtained from CG models to make rapid predictions about the equilibrium behavior of dynamic nanodevices, a key advantage to speeding up the design process. More broadly speaking, this work establishes a methodology for the quantitative analysis of nanomechanical DNA devices and the rational design of next-generation dynamic DNA nanomachines with programmed mechanical behavior.

## RESULTS

**Equilibrium Conformations.** We first tested whether our MD simulations of the five DNA-origami hinge designs (with different spring lengths) based on the oxDNA model (Figure 1b) could predict the equilibrium angle distributions obtained from transmission electron microscopy (TEM) images of the experimental hinges.<sup>18</sup> Representative snapshots of the hinges captured from the simulations are shown in Figure 2a. The “hinge angle”  $\Phi$  was calculated as the angle subtended between linear fits through the two hinge arms in accordance with the experimental definition.<sup>18</sup> Using this definition we computed the distribution of bending angles exhibited by each hinge design (Figure 2b). The angle distributions exhibit roughly Gaussian shapes with a standard deviation that seems to increase as the length of the spring increases from 0 to 74 bases, consistent with experiments. Furthermore, a clear shift toward larger  $\Phi$  with increasing spring length is observed, also consistent with experiments. A qualitative comparison of these distributions against those gathered from experiments reveals good agreement (Figure S1).

To more quantitatively compare the simulated and experimental hinge angle distributions, we determined Gaussian fits of each distribution and obtained: the location of their peaks  $\Phi_0$ , denoting hinge “equilibrium” angles, and their full-width-at-half-maximum (FWHM), characterizing the size of bending fluctuations exhibited by each hinge. The equilibrium angles obtained from simulations show excellent agreement with the corresponding angles obtained from experiments (Figure 2c), except for the 0b hinges, where simulations overpredict the experimentally observed angle by roughly 10°. The FWHM values obtained from simulations also show good overall agreement with the experimentally obtained values, though the simulations seem to always underpredict experiments by 1° to 8° (Figure 2c inset). We also investigated whether the CanDo software<sup>13,14</sup> could predict the equilibrium hinge angles based on an underlying finite elements description of rigid components and a worm-like-chain description of flexible components. While the computed angles reproduce the experimental trend of increasing  $\Phi_0$  with spring length, the angle predictions are much smaller than the experimental angles (Figure S2). Thus, for dynamic DNA nanostructures such as the DNA hinges examined here, CG modeling and simulations seems to be a viable approach for predicting both equilibrium conformations and their fluctuations.

The slight discrepancy in the predicted and experimentally measured bending angle of 0b hinges (Figure 2c) is likely related to the especially strong deformation exhibited by these hinges. Specifically, in these hinges, the three lowestmost springs connecting the two hinge arms are effectively dsDNA helices harboring a single nick in the middle (see Figure S3 or the

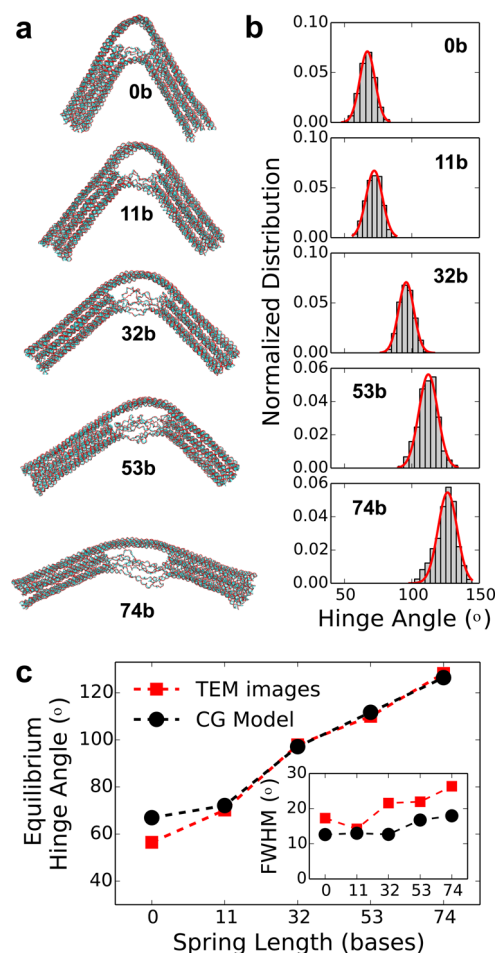


**Figure 2.** Hinge angles  $\Phi$  predicted from MD simulations. (a) Representative snapshots of CG DNA hinges captured from simulations of the five hinge designs (with springs of lengths 0, 11, 32, 53, and 74 bases). (b) Normalized distribution of hinge angles obtained from simulations. Red lines represent Gaussian fits to the distributions. (c) Comparison of the equilibrium hinge angle  $\Phi_0$  and the size of angle fluctuations for the five designs obtained from simulations versus those measured experimentally. Statistical uncertainties in  $\Phi_0$  and FWHM are smaller than the symbol size.

origami designs provided in Supporting Information). To yield the small bending angles, these nicked dsDNA connections have to undergo a large deformation over a short  $\sim 10$ bp stretch. We speculate that the experimental hinges accommodate this large deformation by forming a sharp kink at the nick, which is likely facilitated by the rearrangement of internal bond and torsional angles of the nucleotides and/or by the formation of noncanonical base pairing and stacking interactions. These finer-scale effects are not properly captured in the oxDNA model due to its low resolution and the rigid nature of its nucleotides. We therefore propose that some of the strong bending in these connections is achieved by other deformations, most likely by their bending at the exit points of the hinge arms, where the connections are not directly connected to other dsDNA helices of the hinge arms (see Figure S3). Such bending increases the effective length of the connections, leading to a slight increase in the hinge angle of the oxDNA model as compared to experiments. The reason for the smaller angular fluctuations exhibited by simulations as compared to experiments (Figure 2c inset) is even less clear. We speculate that such difference may arise from minor defects

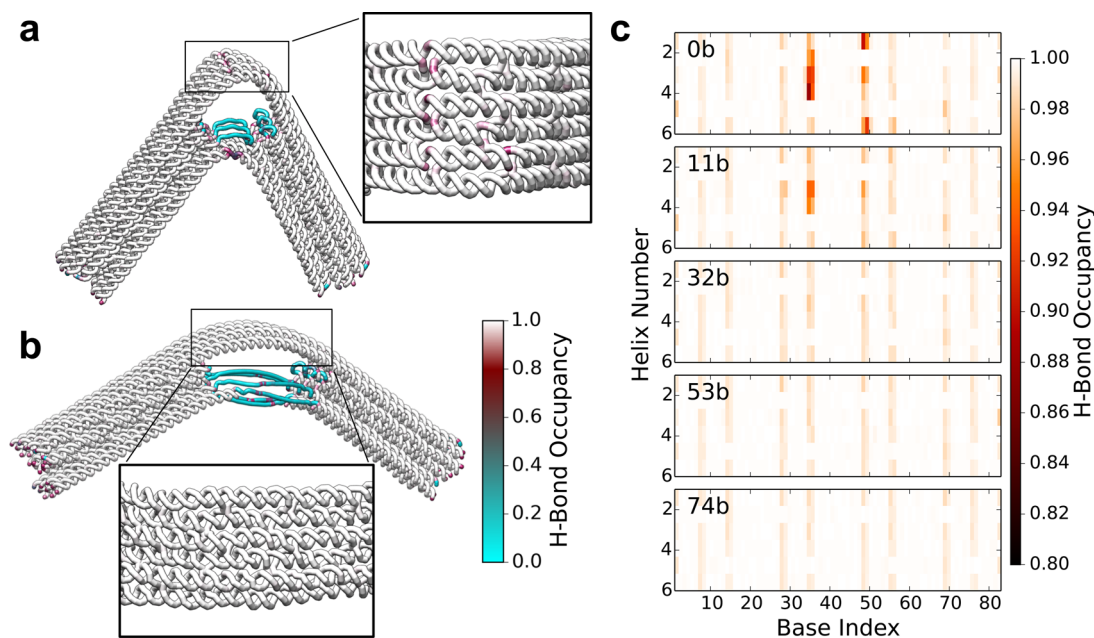


**Figure 3.** Stability of DNA base-pairing interactions within the origami hinges. (a–b) DNA-backbone representation of the hinges with (a) 0b-long springs and (b) 74b-long springs, colored according to the fraction of time their nucleotide bases remain bonded to their complementary bases (H-bond occupancy). Cyan-, red-, and white-colored regions indicate unpaired, weakly paired, and strongly paired bases. (c) Two-dimensional map showing H-bond occupancy of base pairs of the dsDNA helices comprising the hinge joints of all five hinge designs.

in the experimentally assembled hinges or from effects arising from their surface deposition for imaging that might affect the hinge angle distributions.

**Structural Stability.** We evaluated the structural integrity of each hinge design by computing its internal structural fluctuations from the MD simulations, specifically, the root-mean-square fluctuation (RMSF) of the entire hinge as well as of its stiff components (hinge arms) alone. The results, shown for the 0b hinge in Figure S4, demonstrate that the stiff components of the hinges exhibit small structural deviations from the “mean” structure (RMSF  $\approx 5$  Å) and even the entire hinge exhibit relatively small fluctuations (RMSF  $\approx 10$  Å) primarily arising from fluctuations in their dsDNA joints and ssDNA springs. These results suggest that the two hinge arms can be essentially treated as rigid bodies, and therefore the hinge angle  $\Phi$  could indeed be robustly defined based on the angle subtended between the two arms.

To investigate the local stability of the hinges, we computed the fraction of time each nucleotide base remained paired to another base within the hinge across all simulations; bases were considered as “paired” when their mutual interaction energy was negative and had a magnitude greater than the thermal energy  $k_B T$ , where  $k_B$  is the Boltzmann constant and  $T$  is the temperature. This fraction termed “H-bond occupancy” provides a local measure of the stability of double-stranded portions of the hinge (arms and joint), and it also provides a measure of potentially disruptive nonspecific interactions between single-stranded portions of the hinge (springs). The H-bond occupancies of the 0b and 74b hinges are shown mapped onto their corresponding structures in Figure 3a and 3b, and the occupancies of the remaining three designs are provided in Figure S5. Apart from some fraying observed at the open ends of the hinge arms, as indicated by red and cyan spots in the figure, the dsDNA helices of the arms in all five hinge designs remain base-paired most (>95%) of the time, as noted from the uniformly white color of the arms in the figures. We

also observe that the hinge joints remain fully base-paired in most hinges except the 0b-hinge, where some unpairing of bases is observed at locations where the joint undergoes sharp bending. The ssDNA springs, whose sequences were designed to exhibit minimal interactions among each other, remain largely unpaired as expected, except for some base-pairing at intermittent locations along the springs, likely due to self-folding of ssDNA strands. Also as expected, the 4- and 18-bases long ssDNA loops lining the inner ends of the two hinge arms (as required by DNA origami) remain unpaired. Figure 3c provides a more detailed base-wise map of H-bond occupancy in each of the six dsDNA helices making up the joints in the five hinge designs. The maps confirm the stronger unpairing of bases in the 0b hinge joint, and to some extent the 11b hinge joints. The maps further reveal streaks of base unpairing, albeit small, at 7-base intervals in all five hinge designs whose locations correspond to the crossover junctions. These locations naturally lead to weak stacking interactions between adjacent bases on the DNA backbone (Figure S6). Taken together, all hinge designs are structurally stable and do not seem to contain any obvious unstable regions that could trigger more global instabilities.

To further investigate differences in the conformation of the joints across the different hinge designs, we evaluated the local bending of the dsDNA helices comprising the joints. As depicted in Figure 4a, the local bending was characterized in terms of the angle  $\theta_i$  (at each base  $i$ ) subtended by the displacement vectors  $(\mathbf{r}_i - \mathbf{r}_{i-1})$  and  $(\mathbf{r}_{i+1} - \mathbf{r}_i)$  connecting positions  $\mathbf{r}_{i-1}$ ,  $\mathbf{r}_i$ , and  $\mathbf{r}_{i+1}$  of the center of masses of three adjacent base pairs along a DNA helix. The resulting bending angle profiles for each of the six dsDNA helices comprising a joint are plotted in Figure 4b. The profiles reveal a uniform bending angle of  $\sim 12^\circ$  interspersed with near-periodic, sharp peaks suggesting strong bending (kinking) of dsDNA helices at specific locations along the joint helices. Examination of the topology of the layer of 6 helices in the joint (Figure 4c) reveals

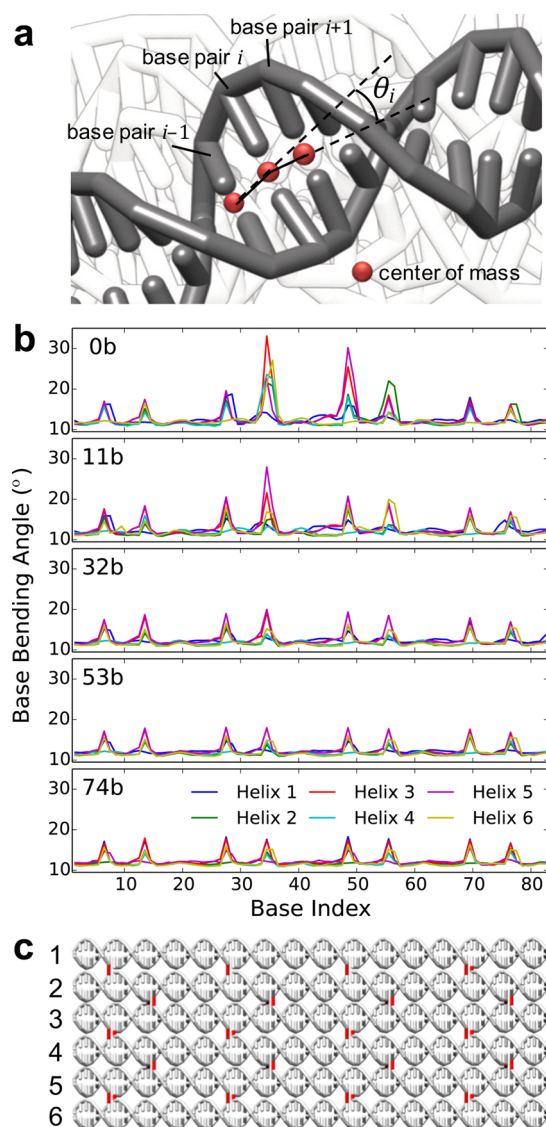


**Figure 4.** Local bending of the hinge joints. (a) Schematic illustrating the calculation of basewise bending angle of the dsDNA helices comprising the joints. (b) Bending-angle profiles of the six dsDNA helices comprising hinge joints, plotted for the five hinge designs. (c) Schematic of the 6-helix joint design showing helix numbering and the position of crossovers between dsDNA helices as marked by red lines.

that these kinks occur at the locations of the crossover junctions, where the staple ssDNA strands cross over from one dsDNA helix to another. These interhelix connections effectively result in nicks in the joint, making those locations easier to bend; These junctions are also responsible for the near-periodic streaks of base unpairing observed in Figure 3c. We also note that the bending angle peaks are especially large for the 0b and 11b hinges close to the middle of the joint, obviously occurring due to the more constricted hinge angle  $\Phi$  exhibited by these two hinges with short springs (Figure 2c). As discussed in other studies,<sup>46</sup> dsDNA subjected to strong bending forces can more effectively relax (minimize its free energy) by forming sharp kinks rather than bending uniformly across its entire length. Similar kinks were also observed experimentally in the case of 0b hinges.<sup>18</sup> Interestingly, as the joints become increasingly bent (due to springs becoming

shorter), the “baseline” bending angle of  $\sim 12^\circ$  remains largely constant, suggesting that all the bending deformation is essentially accommodated at such kinks, especially those in the middle of the joints.

**Global Motions.** To reveal the most important, large-scale (collective) motions exhibited by the DNA hinges, we carried out principal component analysis (PCA) of the hinge trajectories obtained from MD simulations. This approach decomposes the complex motion of a large molecule such as the hinge into principal components, or modes, each of which is specified by an eigenvector describing the direction of translational motion of that mode and a corresponding eigenvalue describing the amount of structural variance of the molecule captured by that mode. By projecting the simulated conformational dynamics of the hinge onto the eigenvector defined by the few largest principal components, one can obtain a lower-dimensional description of the conformational dynamics of each hinge design.

The PCA analysis reveals that over 70% of the internal variance of the hinges can be described by four principal components (Figure 5e). We confirmed that these dominant modes are relatively uncoupled from each other by computing correlations across them; Representative correlation plots for

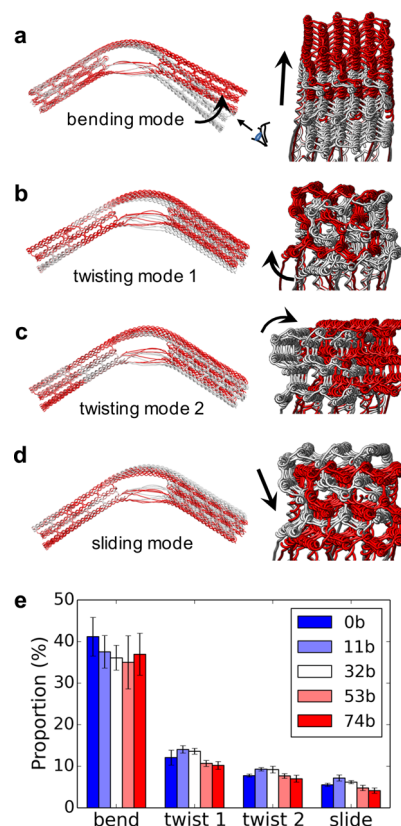


**Figure 5.** Principal component analysis (PCA) of the five hinges. Visualization of the four essential motions exhibited by the hinges revealed by PCA: (a) bending mode, (b,c) two twisting modes, and (d) sliding mode. The hinges are represented by lines joining the center of masses of the DNA bases with the largest and the smallest projections along the principal components depicted in white and red lines. The left and right columns show the front and side views of the four modes. (e) Bar chart showing the relative contribution of each mode toward the dynamics exhibited by each of the five hinges.

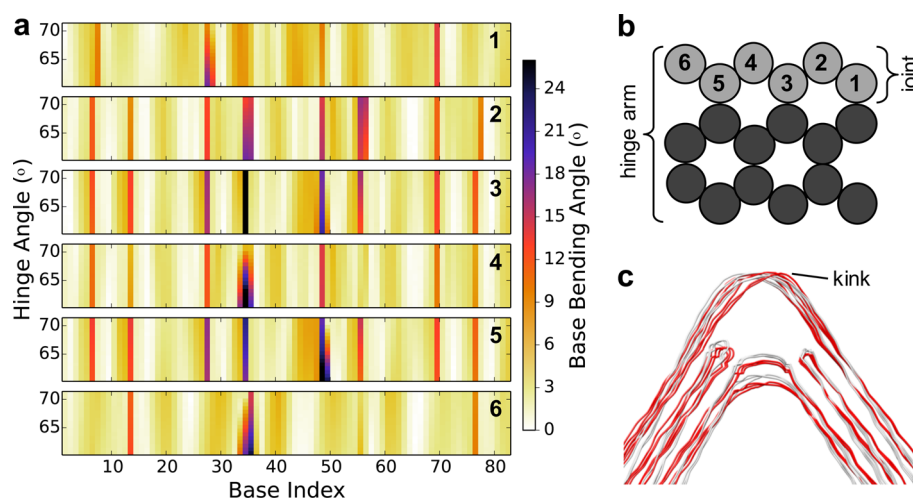


**Figure 6.** Local bending of 0b hinge joint from projections of hinge conformations along the bending-mode principal component (PC). (a) Maps of the basewise bending angle as a function of the hinge bending angle for the six joint helices numbered 1 through 6. (b) Hinge cross section showing the numbering scheme of the six joint helices (gray), and their connections among themselves and with the remaining helices comprising the hinge arms (black). (c) Minimum (white) and maximum hinge angle (red) projections along the bending mode PC illustrating the formation of a sharp kink in the joint. Only the dsDNA axes are shown for clarity.

the 74b-hinge are provided in Figure S7. The most dominant principal component is the bending mode (Figure 5a), contributing about 38% of the hinge variance, followed by two twisting modes (Figure 5b,c) and a sliding mode (Figure 5d), each of which contribute about 5–12% of the variance. Visualization of the four modes, *via* projection of hinge dynamics along the eigenvectors corresponding to each mode, reveals that the bending mode represents in-plane, flexion-extension of one arm relative to the other while maintaining the end-to-end extension of the springs or the joint almost fixed, and it thus represents the mode most responsible for altering the hinge angle  $\Phi$ . The two twisting modes are visualized as off-centered clockwise orbiting of a hinge arm relative to the other about different centers, motions that lead to only minor changes in  $\Phi$  and in the joint and spring extensions. Finally, the sliding mode is visualized as a diagonal shift in the position of one arm relative to the other, with some change in the length of the springs and the joint but minor changes in  $\Phi$ . These mode projections further reveal that the stiff arms preserve their internal structure across all four modes, consistent with our earlier RMSF analysis (Figure S4). The projections also reveal that, on average, the springs belonging to the 74b-hinge extrude out much more significantly as compared to those of the 0b-hinge, evidently due to strong electrostatic and entropic repulsive interactions between the longer springs (Figure S8). We also note that the net proportion of variance accounted by these four modes is smaller for the long-spring hinges compared to the hinges with short springs, which is also consistent with the fact that hinges with longer springs have higher flexibility in general (Figure 5e).

Given that the bending mode is most responsible for the variations in hinge angle  $\Phi$ , the PCA projections of hinge dynamics along this mode provide an excellent opportunity to more extensively study the bending of the joints; Such projections also have the potential to reveal trends that are often difficult to glean from the raw MD trajectories where large thermal fluctuations mask subtle variations in global conformations and motions. We therefore carried out bending-angle calculations on these bending mode projections similar to that carried out earlier on the hinge conformations obtained

from MD simulations. The results for 0b hinges are plotted in Figure 6a and show that the locations of the kinks coincide with those of the crossover junctions (Figure 4c) and relate well to the results obtained from MD trajectories (Figure 4b). Accordingly, the middle-four joint helices, which carry more crossover junctions than the two end helices (Figure 4c), exhibit a larger number of kinks. Since the bending deformation is now distributed over a larger number of kinks, the kinks in the middle helices are expectedly weaker than those in the end helices. Among the two end helices numbered 1 and 6, helix 1 exhibits a smaller increase in the bending angle of its kinks as compared with helix 6. The reason is that the former is connected to two neighboring helices, while the latter is connected only to a single neighboring helix, making the conformation of helix 1 somewhat more restricted compared to helix 6 (Figure 6b). Interestingly, this analysis could also reveal that the kinks in the joint helices become sharper with decreasing hinge angle  $\Phi$ , as noted from the increase in the bending angles of several of the kinks in going from large to small angles. This effect is easily visualized in Figure 6c, which displays two extreme projections of the 0b-hinge, where one of the kinks is found to become extremely sharp at small hinge angles. Finally, we note subtle differences in local bending deformations across the six helices composing the hinge joints, also observed in local bending angle profiles Figure 4b, which likely arise from the additional twisting and sliding degrees of freedom exhibited by the hinges.

**Large Deformation Behavior.** Our MD simulations indicate that all hinge designs undergo relatively small fluctuations in the hinge angle at equilibrium, with FWHM values, in the range  $\sim 10$ – $20^\circ$ . However, it is conceivable that future applications of such structures may require them to be subjected to strong external forces that considerably deform them beyond their equilibrium conformations. To investigate the behavior of the hinges under larger deformations that result in more strongly bent or flexed arms (beyond equilibrium fluctuations), we performed “restrained” MD simulations. In these simulations, the deformations were enforced by applying a stiff harmonic potential to the two hinge arms that strongly constrained their center-of-mass separation distance. By

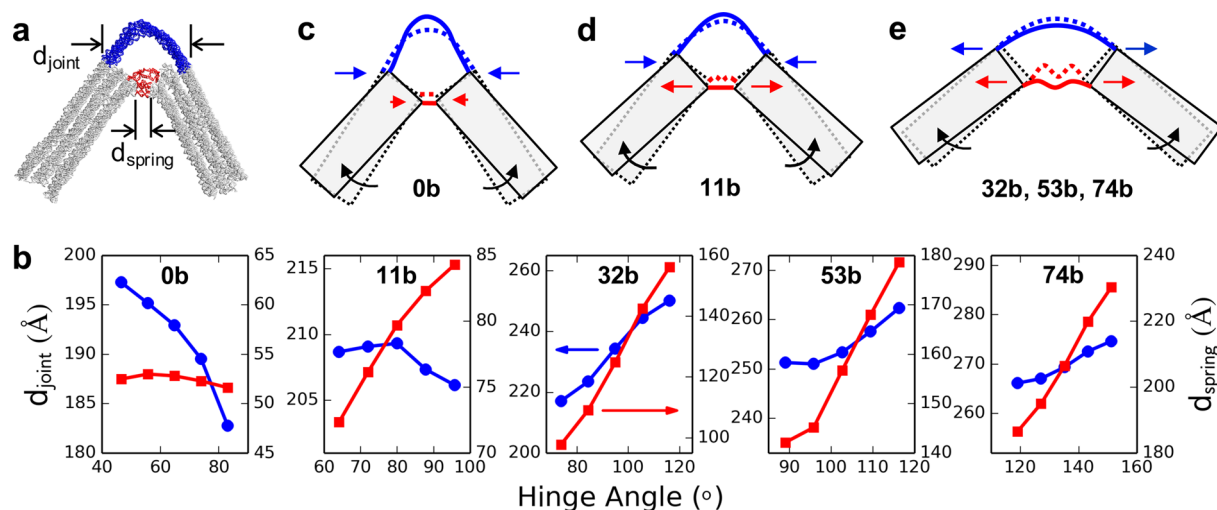


**Figure 7.** Hinge bending behavior under large deformations. (a) CG hinge highlighting the end-to-end distances  $d_{\text{joint}}$  and  $d_{\text{spring}}$  of the joint (blue) and the springs (red). (b) Variations in  $d_{\text{joint}}$  (blue) and  $d_{\text{spring}}$  (red) with hinge angle for the five hinge designs. (c–e) Schematics explaining differences in the bending behavior of (c) 0b, (d) 11b, and (e) 32b, 53b, and 74b hinges. Blue and red arrows depict direction of changes in  $d_{\text{joint}}$  and  $d_{\text{spring}}$  in response to the increase in hinge angle depicted by the curved black arrows; Small arrows imply minor changes. Dashed and solid lines show initial and final configurations of the hinge for increasing hinge angle.

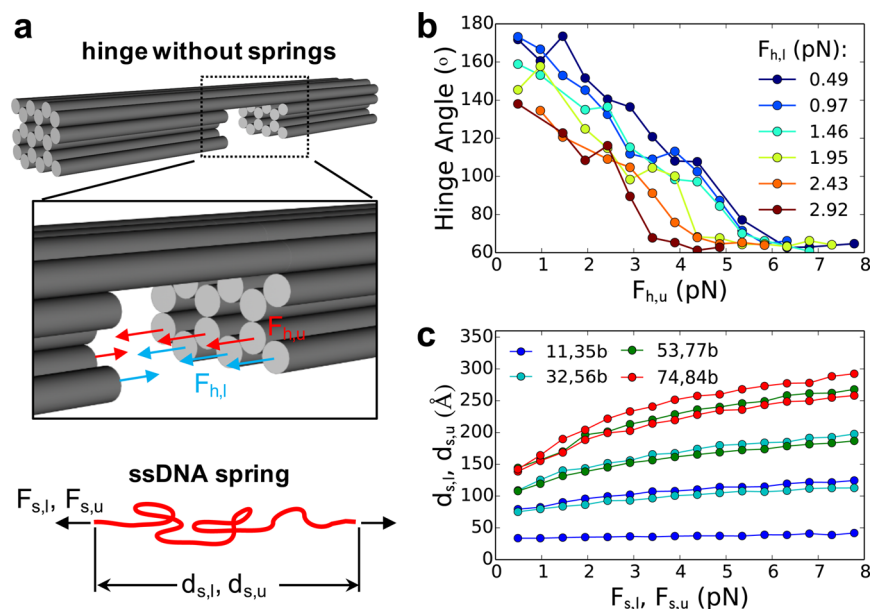


**Figure 8.** Force-deformation behavior of the joint and spring components of the hinge. (a) Schematic showing partitioning of the hinge into its two load-bearing components—the joint (hinge without springs) and the springs—whose force-deformations are treated separately. (b) Force-deformation profiles of the springless hinge for different combinations of force loads  $F_{h,u}$  and  $F_{h,l}$  applied to the upper and lower layer of dsDNA helices, which substitute the effects of the springs. (c) Force–extension behavior of the lower and upper ssDNA springs corresponding to the 11b, 32b, 53b, and 74b hinges.

performing multiple such simulations, each constraining the hinge arms to different distances, we were able to obtain hinge conformations at different extents of deformation, spanning both smaller and larger hinge angles  $\Phi$  than the equilibrium angle. We then monitored how the ensuing equilibrated end-to-end distances of the joint and the springs varied with respect to the enforced hinge angle (Figure 7a).

Figure 7b presents these variations in the joint and spring end-to-end distances as a function of hinge angle for the five hinge designs. We observe three kinds of behaviors: In the case of the 0b hinge, an increase in hinge angle results in a visible decrease in the joint end-to-end distance and a marginal

decrease in the spring end-to-end distance. For the 11b hinges, the spring end-to-end distance increases with increase in hinge angle, but the joint end-to-end distance shows a biphasic response, where the distance shows a rising trend with increasing angle for small angles ( $\Phi < 80^\circ$ ) but a decreasing trend for larger angles. For the remaining hinges (with longer 32b, 53b, and 74b springs), both the joint and spring end-to-end distances increase with an increase in the hinge angle.

The above differences in hinge-bending behavior are intrinsically related to the length of ssDNA springs and the hinge angle. When the springs are sufficiently long, as in the case of the 32b, 53b, and 74b hinges, the hinge arms behave like

two rigid bodies rotating about the center of the joint, as shown schematically in Figure 7e, which leads to the *simultaneous* extension (or compression) of the springs and joints observed in Figure 7b. The joint helices are weakly bent in these hinges and hence the joint is expected to bend uniformly like a Euler elastic beam, as suggested earlier.<sup>18</sup> Moreover, the springs undergo appreciable stretching with increasing angle, which suggests that the springs in these hinges exhibit a somewhat loose conformation at the equilibrium bending angle, as confirmed by the representative structures shown in Figure 2a.

The situation is fundamentally different in 0b hinges, where the springs are entirely double-stranded and thereby effectively incapable of stretching or shrinking. Consequently, all changes in hinge angle occur through rotation of the hinge arms about these dsDNA springs, and hence an increase in  $\Phi$  leads to shrinkage in the joint end-to-end distance, as depicted schematically in Figure 7c. Such end-to-end compression of the joint, combined with the additional constraint on the tangential emergence of joint helices from the hinge arms, leads to strong kinking of the joint helices that are already significantly bent as a result of the short springs. Such strong kinking of the joint helices cannot be treated using continuum mechanical Euler elastic beam model.

Lastly, the 11b hinges behave intermediate to the above two sets of hinges in that they exhibit a switch from one bending behavior to the other (Figure 7b). At small hinge angles, the springs are relatively loose and are capable of some stretching and the increase in bending angle occurs through rotation of hinge arms through the joint center, leading to simultaneous increase in both joint and spring distances. However, at large angle, the springs become taut and incapable of stretching further, leading to the rotation of hinge arms through the springs rather than the joint center and a subsequent decrease in the joint distance, as depicted in Figure 7d. This also leads to introduction of a kink in the joint, albeit of smaller magnitude than that observed in 0b hinges.

**Hinge Angle Predictions from Force-Balance.** In classical mechanics, a multicomponent system is considered to be at mechanical equilibrium when the net force and torque acting on all components is zero. The equilibrium conformation of the system can then be determined from “force-balance” and “torque-balance” conditions, that is, the force and torque one component exerts on another component through their connection point(s) is equal and opposite to the force and torque the second component exerts on the first component. We examined if such a force- and torque-balance formalism could be used to predict the equilibrium conformations of our nanoscopic DNA hinges, that is, the equilibrium bending angles  $\Phi_0$  plotted in Figure 2c. To this end, we divided the hinge into two components: (i) the six ssDNA springs that connect the lower portions of the two hinge arms, and (ii) the rest of the hinge without springs consisting of the joint and the rigid hinge arms (Figure 8a). The first component, the springs, experience outward-pointing forces (tension) at their ends due to the bent joint attempting to straighten out the hinge arms. Though electrostatic repulsion between the arms may also contribute to this force, our calculations suggest that the repulsion is minimal (Figure S9), likely due to the high salt concentration used in simulations and experiments that essentially screens most electrostatic interactions. The second component, the springless hinge, experiences inward-pointing forces (compression) on the hinge arms at locations of spring attachment due to stretching of the springs. Interestingly, the torque-balance

condition is automatically satisfied as the two components exert zero torque on each other due to symmetry: the springs exert equal and opposite forces on the two hinge arms at exactly apposite points and the springless hinge also exerts equal and opposite forces to the ends of the springs. Hence, only the force-balance condition is required, and the equilibrium angle  $\Phi_0$  of the hinges may be determined from the individual force-deformation behavior of the two hinge components, regardless of the origin of the forces, as the angle at which the corresponding deformations of the two components yield exactly the same force.

The force-deformation behavior of the springless hinges were determined by substituting each spring with a pair of forces applied to the DNA bases on the two hinge arms connected to the springs in the original design (Figure 8a top). However, all springs are *not* alike, as the three springs connected to the upper set of hinge arm helices are 24 bases longer than the three connected to the lower set of helices (except for the 74b hinges where the two sets of springs are of lengths 74 and 84 bases). Thus, the forces replacing the two sets of springs should be treated separately, which we denote by  $F_{h,l}$  and  $F_{h,u}$  for the lower and upper set of springs (depicted by blue and red arrows in Figure 8a). The force-deformation behavior was obtained by performing a series of MD simulations mapping through various possible combinations of applied forces  $F_{h,l}$  and  $F_{h,u}$  and the resulting deformation was characterized in terms of the hinge angle  $\Phi$ , as defined earlier. Figure 8b presents these force-deformation curves  $\Phi(F_{h,l}, F_{h,u})$  as a function  $F_{h,u}$  for different fixed values of  $F_{h,l}$  showing the expected trend of decreasing hinge angle with increase in either force.

The force-deformation behavior of the lower and upper set of springs corresponding to each hinge design can also be determined from MD simulations by applying a stretching force to the individual springs and measuring their end-to-end distance (Figure 8a bottom). To distinguish between the behaviors of the two kinds of springs, we denote their end-to-end distances by  $d_{s,l}$  and  $d_{s,u}$  and the applied forces by  $F_{s,l}$  and  $F_{s,u}$ . Figure 8c shows the computed force–extension behaviors  $d_{s,l}(F_{s,l})$  and  $d_{s,u}(F_{s,u})$  for the two sets of springs corresponding to the 11b, 32b, 53b, and 74b hinges (the hinge labeling corresponds to the length of the shorter spring). Note that this approach cannot be applied to 0b hinges, which do not contain any ssDNA springs. The profiles show behavior characteristic of polymer stretching that is typically modeled using the worm-like-chain model. As expected, the shorter, lower springs exhibit sharper force–extension behavior compared to the longer, upper springs.

The simulations of the springless hinge also reveal a strong relationship between distances  $d_{s,l}$  and  $d_{s,u}$  across the two sets of spring attachment points on the hinge arms and the hinge angle  $\Phi$  (Figure 9a). These two geometrical relationships denoted by  $d_{s,l}(\Phi)$  and  $d_{s,u}(\Phi)$  are slightly nonlinear, suggesting some deformation of the spring attachment points upon application of force. We also note that hinges cannot contract beyond  $\Phi \approx 60^\circ$ , whereupon the distance between the spring connections points becomes smaller than the length of a single base pair, corresponding to the case of the 0b hinge.

Lastly, the force-balance condition stipulates that at mechanical equilibrium, the magnitude of the spring and hinge forces are identical, *i.e.*,

$$F_{h,u} = F_{s,u} \quad (1)$$

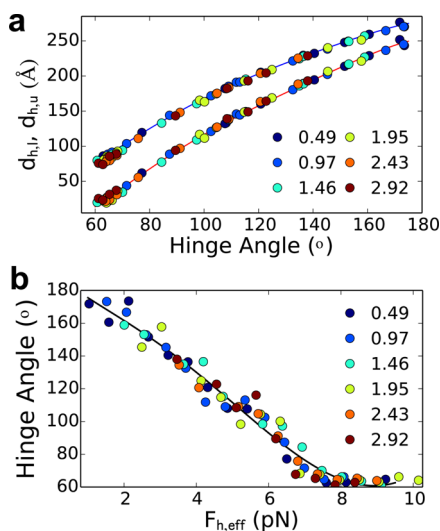


**Figure 9.** Additional relationships required for transforming or simplifying the force-deformation behavior of the springs and the joint. (a) Geometrical relationship between the end-to-end distances of the upper and lower spring-connection points and the hinge angle. (b) Force-coupling relationship  $F_{h,\text{eff}} = F_{h,l} + \lambda F_{h,u}$  with  $\lambda = 1.124$  allows collapse of the joint force-deformation curves in Figure 8b onto a single master curve. Symbols, with the same color scheme as in Figure 8, represent data measured from simulations of the springless hinge conducted at different  $F_{h,u}$  and  $F_{h,l}$ , whereas lines represent polynomial fits to data.

$$F_{h,l} = F_{s,l} \quad (2)$$

The force-deformation profiles  $\Phi(F_{h,l}, F_{h,u})$ ,  $d_{s,l}(F_{s,l})$ , and  $d_{s,u}(F_{s,u})$  along with the geometrical relationships  $d_{s,l}(\Phi)$  and  $d_{s,u}(\Phi)$  and the force-balance constraints (eqs 1 and 2) results in a system of 7 relationships (equations) with 7 unknown variables. Solving these equations then yields the equilibrium hinge angle  $\Phi_0$  we seek. An underlying assumption here is that the springs do not interact with each other, and hence the force–extension behavior of the sets of three springs belonging to one layer can be obtained from the behavior of a single spring using the springs-in-parallel formulation. However, in cases where the springs interact with each other, it may be more correct to simulate groups of springs and compute their collective force–extension behavior.

Due to the dependence of the hinge angle on two variables ( $F_{s,l}$  and  $F_{s,u}$ ) and the need to satisfy two force-balance conditions (eqs 1 and 2), solving for the equilibrium angle  $\Phi_0$  becomes convoluted and requires an iterative numerical approach. To simplify the solution process, we investigated whether the two sets of forces could be combined into a single effective force. The rationale is that even though the effects of the lower and upper layer of springs are treated separately using two different forces, the equilibrium hinge angle results from their combined effect on the hinge arms. Specifically,  $F_{h,l}$  and  $F_{h,u}$  exert separate moments on the joint ends via the hinge arms, with the former exerting a larger moment due to the larger moment arm associated with that force. Hence, we proposed that the two forces could be coupled together through a factor  $\lambda$ , resulting in an effective force

$$F_{h,\text{eff}} = F_{h,u} + \lambda F_{h,l} \quad (3)$$

which, when applied to the upper layer of helices, should produce the same hinge deformation as the two separate forces

applied to both layers of helices. Geometrically, the coupling factor should be 1.181 according to the ratio of the moment arms of the two force loads with respect to the joint-arm connection point. However, other factors could affect the coupling of forces, such as the deformation of the hinge arms near the springs, as mentioned earlier, and differences in the orientation of the terminal bases of the springs, both of which affect the length of the moment arm. The coupling factor is therefore obtained as a fitting parameter that best collapses all the distinct force-deformation profiles presented in Figure 8b onto a single “master” curve. The fitted value  $\lambda = 1.124$  is quite close to the geometric prediction, implying that the aforementioned factors affecting the moment arms of the two force loads are not significant. Figure 9b shows the collapsed force-deformation  $F_{h,\text{eff}}-\Phi$  plot demonstrating that the effect of the two applied forces (two sets of springs) can indeed be treated in terms of a single effective force.

This ability to couple the two spring forces applied to the hinge arms into a single effective force load greatly simplifies the solution of  $\Phi_0$ . First, the original 2D force-deformation landscape  $\Phi(F_{h,l}, F_{h,u})$  of the springless hinge is now replaced by a 1D force-deformation master curve  $\Phi(F_{h,\text{eff}})$ , where the effective force is obtained via eq 3. Second, the original two force-balance conditions (eqs 1 and 2) are now replaced by a single effective force-balance condition

$$F_{h,\text{eff}} = F_{s,\text{eff}} \quad (4)$$

where  $F_{s,\text{eff}}$  represents the effective force exerted by the two sets of springs based on the coupling factor determined earlier as given by

$$F_{s,\text{eff}} = F_{s,u} + \lambda F_{s,l} \quad (5)$$

In this revised setup, one needs to solve a different set of 7 single-variable equations with 7 unknowns, namely, the force-deformation curves  $\Phi(F_{h,\text{eff}})$ ,  $d_{s,l}(F_{s,l})$ , and  $d_{s,u}(F_{s,u})$ ; the geometrical relationships  $d_{s,l}(\Phi)$  and  $d_{s,u}(\Phi)$ ; the effective force-balance condition given by eq 4, and the coupling relationship given by eq 5. Once the force-deformation curves of the springless hinge  $F_{h,\text{eff}}(\Phi)$  and of the two sets of springs and  $F_{s,l}(d_{s,l})$  and  $F_{s,u}(d_{s,u})$  have been obtained, the protocol for obtaining  $\Phi_0$  becomes fairly straightforward: The  $F_{s,l}(d_{s,l})$  and  $F_{s,u}(d_{s,u})$  curves are first converted to  $F_{s,u}(\Phi)$  and  $F_{s,l}(\Phi)$  curves via the geometrical relationships  $d_{s,l}(\Phi)$  and  $d_{s,u}(\Phi)$ . The two curves are then combined into a single  $F_{s,\text{eff}}(\Phi)$  curve via the coupling factor (eq 5). The intersection between the resulting  $F_{s,\text{eff}}(\Phi)$  and  $F_{h,\text{eff}}(\Phi)$  curves, signifying the use of the force-balance constraint (eq 4), then yields the equilibrium hinge angle  $\Phi_0$ .

Figure 10a presents the force-deformation master curve  $F_{h,\text{eff}}(\Phi)$  of the springless hinge along with the transformed force-deformation curves  $F_{s,\text{eff}}(\Phi)$  of the springs corresponding to the 11b, 32b, 53b, and 74b hinges. The intersections of the two curves allows us to estimate the equilibrium hinge angle for the hinges with the certain ssDNA spring length. The predicted results shown in Figure 10b are in excellent agreement with both the experimentally measured hinge angles and those computed earlier from simulations of entire hinges. The promising nature of these results suggests that it may indeed be possible to predict the equilibrium conformation of a multicomponent DNA nanostructure from the force-deformation behavior of its individual components. In this study, we obtained such behavior from MD simulations of the

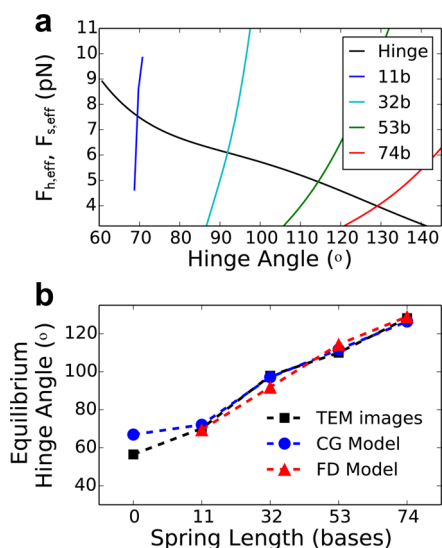


**Figure 10.** Equilibrium hinge angle from force-deformation (FD) behavior. (a) Transformed FD curves of the springless hinge and of the 11b, 32b, 53b, and 74b springs. (b) Equilibrium hinge angles as obtained from the intersection points of the transformed spring and hinge FD profiles compared to those obtained from simulations and experiments. Statistical uncertainties in  $\Phi_0$  are smaller than the symbol size.

components in isolation though, in principle, the components-level behavior could also be obtained experimentally.

## DISCUSSION

This study provides a detailed picture of the nanoscopic structural dynamics exhibited by a set of mechanically compliant nanostructures fabricated *via* DNA origami—hinges with tunable bending angle designed by combining rigid DNA bundles with semirigid and flexible DNA elements. Our approach involved performing MD simulations of the DNA hinges treated using the *oxDNA* CG force field developed by the Ouldrige, Doye, and Louis laboratories. One of the goals of this study was to determine whether such a modeling approach could even capture the overall conformations of the hinges determined experimentally from electron microscopy. Our results show that the *oxDNA* model does reasonably well in reproducing the experimentally measured distributions of hinge bending angles for a range of hinge designs, especially the equilibrium angles denoted by the peaks in the angle distributions. This result is significant because the hinges are flexible and exhibit thermal fluctuations, and are thus not amenable to modeling *via* continuum-mechanics approaches that have found success in modeling other more rigid DNA nanostructures. At the same time, the hinges are too large and undergo slow bending dynamics, making all-atom MD simulations computationally prohibitive for probing such dynamics. Hence, coarse-grained models that ignore fine-scale features and degrees of freedom while still accounting for important geometrical features, molecular interactions, and thermal fluctuations offer the only practically viable solution for probing the dynamics of such structures. Indeed, the *oxDNA* simulations required 14 h CPU time on NVIDIA GPUs to simulate 100  $\mu$ s-long dynamics of the hinges, almost 5 orders of magnitude faster than all-atom MD simulations of the hinges in explicit solvent. The promising predictions made by the *oxDNA* model here suggests that such a CG modeling and

simulation approach could be a useful tool for elucidating and predicting the dynamics of devices created *via* DNA nanotechnology and that such a tool could become an important component of computer aided design of such DNA devices. Needless to say, the approach would first have to be thoroughly tested and validated against other DNA nanostructures undergoing more complex dynamics or other kinds of conformational changes. Also, the approach would need to become more readily accessible to researchers in DNA nanotechnology who might not be experts in MD simulations.

Nevertheless, having established the predictive capability of *oxDNA* for the DNA hinges, we next used it to probe their intricate structure and dynamics. We found that in all hinge designs, the hinge arms composed of DNA helix bundles remained structurally intact during the simulations while exhibiting  $\pm 5$ – $8^\circ$  fluctuations about their equilibrium bending angle. By computing the fraction of time DNA nucleotide bases remain paired, we determined regions of local instability within the double-stranded portions of the hinge. Apart from obvious fraying of bases at the open ends of the hinge-arm helices, the dsDNA helices in both the hinge arms and the joints remained fairly stable throughout the simulations. Interestingly, the hinge joints display localized, near-periodic streaks of slightly less stable base-pairing interactions that coincide with the crossover points of the DNA staples. Analysis of the local bending of the joint helices revealed that the helices bend more-or-less uniformly across their length, except at crossover junctions where they exhibit a relatively larger bending angle. These “kinks” in the joints become very sharp near the midpoint of the joint, especially for the 0b hinges designed to exhibit a small bending angle. Such strong kinking of the dsDNA helices in strongly bent joints is reminiscent of the kinks observed in the dsDNA wrapped around the histone octamer within nucleosomes, where the strong histone/DNA interactions lead to very strong superhelical bending of DNA.<sup>47</sup>

Principal component analyses of the simulation trajectories of the hinges allowed us to extract their most dominant global motions. Our results show that while the dynamics of the hinges are dominated by the planar bending of arms relative to each other, other dynamic modes such as relative twisting and sliding of arms are also important. While such secondary modes could be considered as a disadvantage in applications where precise motion along a single degree of freedom is required, the modes may also be considered as a unique advantage of these soft DNA-based devices, and this type of analyses could enable specific design of thermal fluctuations along multiple degrees of freedom. Indeed most naturally occurring nanomachines such as protein enzymes and molecular motors exhibit some degree of flexibility or softness along multiple degrees of motion that is often a critical part of the mechanical function. In the macroscopic world, the observed flexibility of hinges is remarkably similar to the knee joint in humans, which has primarily evolved to exhibit the bending degree of freedom, though other smaller rotations and sliding motions also occur that are in fact critical for the functionality and strength of the knee joint.

Examining the behavior of hinges subjected to strong deformation revealed that the hinges with sufficiently long ssDNA springs (>11 bases) exhibit bending behavior typical of joints, that is, extending the hinge angle leads to an increase in the end-to-end extension of both the joint and the springs, typical of the hinge arms rotating about the joint center to extend or flex. However, the 0b hinges, and to some extent the

11b hinges, exhibit fundamentally different behavior with the end-to-end extension of the joint decreasing, rather than increasing, with increasing hinge angle. This effect arises due to the near-inextensible nature of short ssDNA springs that forces the hinge arms to flex or extend about the ssDNA connection points rather than the joint center. Due to the constraint on the orientation of the two ends of the joints as a result of their connection to the hinge arms, their opening up causes counterintuitive stronger-than-usual bending of the joints, leading to sharp kinking of the joint helices. Interestingly, such “auxetic” behavior with expansion in one dimension leading to expansion in the other dimension (as opposed to contraction, typical of most materials) could serve as a basis for the design of materials that exhibit in-plane or 3D negative Poisson’s ratio.

We finally investigated if the equilibrium bending angles of the hinges could be predicted by combined analysis of its individual components using the force-balance principle commonly applied in continuum mechanics. To this end, we divided the hinge into two simpler mechanical components, the ssDNA springs and the remaining hinge minus the springs, and computed their individual force-deformation behaviors. By invoking the force balance conditions along with the geometric relationship between spring and hinge deformation, we were able to make excellent predictions of the hinge angle. Apart from demonstrating the applicability of a key principle of classical mechanics to a strongly fluctuating nanoscale device, the ability to predict the mechanical behavior of DNA devices from the behavior of their individual components would benefit the design of complex devices. In addition to simplifying the design process, it would save significant computational effort, for instance, when examining the behavior of device designs obtained from combinations of components with different properties. In the context of hinge design, predicting the behavior of all hinges assembled from  $m$  possible joint designs and  $n$  possible spring designs would nominally require  $m \times n$  MD simulations of the full hinges, whereas the components-level design would require only  $m + n$  simulations of the components, that is, fewer simulations of smaller systems. This framework is also amenable to a modular design framework where interchangeable components can be screened through a mechanical system to produce the desired overall mechanical behavior. Note that springs and joint design parameters are not just restricted to their lengths, as examined in this work, but also changes in the material itself. For instance, the ssDNA springs could be replaced by ssDNA-dsDNA segments, azobenzene-tethered DNA segments,<sup>48</sup> or other polymers.<sup>49</sup>

## CONCLUSIONS

We have used CG MD simulations to study the conformational dynamics of DNA origami hinges at the molecular scale. Our results show good agreement between the predicted and experimentally measured hinge-angle distributions for a range of hinge designs. The simulations also revealed various nanoscopic properties of the hinges that may be difficult to obtain experimentally, such as their local mechanical stability, detailed conformations, collective motions, and design-dependent bending mechanism. Lastly, we proposed an approach for predicting equilibrium hinge angles based on microscopic force-deformation behaviors of the single- and double-stranded components and macroscopic conditions of mechanical equilibrium, providing a potentially rapid yet reliable means of predicting the equilibrium conformation of multicomponent

DNA nanostructures. This work thus lays the foundation for understanding and predicting the mechanical behavior of other dynamic DNA nanostructures where continuum mechanics and all-atom models become inapplicable or computationally expensive. This work also sets ground for future work on designing mechanisms to actuate such structures for nanoscale sensing and mechanical engineering applications. For instance, the DNA hinges studied here could be engineered to trigger bending angle changes *via* design of displacement ssDNA strands that hybridize with the ssDNA springs to either flex or extend the hinges or *via* other responsive entities such as azobenzene-tethered DNA that respond to light to trigger a conformational change in the springs or the joints. The CG modeling approach tested here should aid in the design and optimization of such actuation mechanisms, and the components-level modeling strategy introduced here should further help speed up the process of design.

## METHODS

**Hinge Designs.** The five DNA origami hinge designs, referred to as 0b, 11b, 32b, 53b, and 74b hinges, were built on a honeycomb lattice in the caDNAno package;<sup>11</sup> The designs are provided in the Supporting Information (Figure S10–S14). The joint DNA helices in each of the five hinge designs are 84 bp long. The two layers of springs are of lengths 0 and 24 bases in the 0b hinge; 11 and 35 bases in the 11b hinge; 32 and 56 bases in the 32b hinge; 53 and 77 bases in the 53b hinge; and 74 and 84 bases in the 74b hinge. Since the 18-helix DNA bundles composing the hinge arms essentially behave like rigid components and also exhibit negligible electrostatic repulsion between them (Figure S8), the length of the two hinge arms were reduced from ~220 bases in the experimental design to ~96 bases in our simulations; This allowed us simulate the hinges and predict their properties at significantly reduced computational costs.

**OxDNA Model.** The DNA hinges were modeled using oxDNA2,<sup>50</sup> an updated version of the oxDNA model.<sup>33</sup> In this model, each DNA strand is treated as a chain of rigid bodies representing nucleotides, and the surrounding solvent and ions are treated implicitly. Each nucleotide is represented by three interaction sites—one site for each pair of phosphate and sugar groups and two sites for each base. The noncollinearity of the three interaction sites enables the model to capture the asymmetric shape of the dsDNA helix with distinct major and minor grooves. Each nucleotide is also represented by a vector perpendicular to the notional plane of each base whose direction enables the model to capture the orientational dependence of base-stacking and Watson–Crick base-pairing interactions. The total potential energy of a multistrand system is given by the sum of eight pairwise interaction terms:

$$U_{\text{tot}} = \sum_{\text{nearest neighbors}} (U_{\text{bb}} + U_{\text{stack}} + U'_{\text{ev}}) + \sum_{\text{other pairs}} (U_{\text{HB}} + U_{\text{cs}} + U_{\text{ev}} + U_{\text{coax}} + U_{\text{DH}}) \quad (6)$$

where the first sum accounts for interactions between *adjacent* nucleotides on the same strand, and contains  $U_{\text{bb}}$ ,  $U_{\text{stack}}$ , and  $U'_{\text{ev}}$  terms that describe the connectivity between adjacent backbone sites, stacking interactions across neighboring base sites, and excluded volume interactions between neighboring nucleotide sites, respectively. The second sum accounts for interactions between *all other* pairs of nucleotides in which  $U_{\text{HB}}$  describes hydrogen-bonding interactions between complementary bases,  $U_{\text{cs}}$  describes cross-stacking interactions between bases on opposite DNA strands,  $U_{\text{ev}}$  describes excluded volume interactions,  $U_{\text{coax}}$  describes coaxial stacking of non-neighboring bases on the same strand, and  $U_{\text{DH}}$  describes salt-screened electrostatic interactions between non-neighboring backbone sites. All interaction potentials, except the excluded volume, backbone, and electrostatic terms, depend on the relative orientations of the nucleotides, in addition to depending on distances between interaction

sites. The interaction-potential parameters, such as the location and depth of energy minima, force constants, and charges, were fitted to reproduce experimentally measured properties of DNA: the stacking transition of ssDNA; length- and salt-dependent melting transition curves and melting temperature of short dsDNA duplexes; persistence lengths of ssDNA and dsDNA; and elastic torsional and stretching moduli of dsDNA. Further details on model development, parametrization, and application are provided elsewhere.<sup>33,42,50</sup>

**Generation of Initial Hinge 3D Conformations.** The caDNAno hinge designs were used to generate initial 3D structures of the hinges in which their arms were completely flexed to 180°. However, such initial configurations resulted in abnormal stretching of the centermost phosphate bond in each spring of the hinge. To relax these stretched bonds, the bonds were cut and substituted with harmonic potential restraints of strength 0.4 kcal/mol/Å<sup>2</sup> on the distance between the two bonded nucleotides during structural relaxation; In this process, the equilibrium distance of the restraints was shortened in 6 Å steps every 600 000 MD simulation time steps until the equilibrium bond length was reached through gradual bending of the hinge arms, whereupon the broken bonds were reinstated.

**MD Simulations.** The MD simulations were performed using the oxDNA package at a temperature of 298 K and a monovalent salt concentration of 500 mM Na<sup>+</sup>. The high salt regime were chosen to reproduce the strong electrostatic screening from 14–20 mM Mg<sup>2+</sup> concentrations used to assemble and stabilize the hinges. While oxDNA2 can capture electrostatic screening effects of Mg<sup>2+</sup> through the use of the Debye–Hückel formalism at high Na<sup>+</sup> concentrations, the model is unable to capture finer-scale effects of Mg<sup>2+</sup> ions such as their ability to form coordination complexes. However, such effects do not seem to be critical for DNA hinges, as the hinge angle distributions obtained from simulations conducted at lower Na<sup>+</sup> concentrations (150 mM) were quite similar to those presented here (Figure S15). Furthermore, recent unpublished experiments by Castro and co-workers on a different set of hinges yield quite similar distributions in hinge angle for structures prepared using 600 mM Na<sup>+</sup> and using 25 mM Mg<sup>2+</sup>.

The simulation time step was set to 15.15 fs and an Andersen-like thermostat was used every 103 Newtonian time steps to approximately yield Brownian motion of the DNA structures in water. For all hinge designs, we performed three ~300 ns long MD production runs, each starting from a different initial configuration. These simulation times do not represent physical times due to implicit treatment of the solvent and smoothening of the energy landscape associated with coarse graining, which are expected to cause a speedup in dynamics. The physical time may be obtained by rescaling the simulation time by a factor  $\alpha$  quantifying this speedup, typically approximated as the ratio of the self-diffusivity obtained from simulations to that measured experimentally.<sup>51</sup> OxDNA simulations of a 21-bp dsDNA fragment, with an experimentally measured diffusivity of  $5.3 \times 10^{-7}$  cm<sup>2</sup>/s in solution,<sup>52</sup> yielded a diffusivity of  $1.79 \times 10^{-4}$  cm<sup>2</sup>/s, that is,  $\alpha \approx 330$ . Thus, each of our simulation runs were in fact ~100  $\mu$ s long and each time step represented 5 ps. Also, the simulations were sufficiently long to adequately sample the bending angle fluctuations of the hinges, as noted from time-autocorrelation functions  $\langle(\Phi(t) - \Phi_0)(\Phi(0) - \Phi_0)\rangle$  in the hinge angle computed for the five designs (see Figure S16). In particular, the characteristic relaxation time of the angle fluctuations estimated from exponential fits to the correlation functions (~2–20  $\mu$ s) were all found to be much shorter than the simulation run times.

Since we are more interested in elucidating the effects of structural design rather than sequence design on the hinges' conformational dynamics, we used the average-base parametrization option in oxDNA, whereby average parameters for base-pairing and base-stacking interaction strengths are used. Furthermore, the self-folding of the ssDNA springs was eliminated in each hinge design.

**Principal Component Analysis.** This analysis was performed using the software package *bio3D*.<sup>53</sup> Specifically, we inputted ~500 configurations (snapshots) of the hinge for each design, collected at equal time intervals from the entire 900 ns-long simulation trajectory. Each configuration of the hinge was described using the centers of

masses of its DNA nucleotides; Note that each nucleotide is represented by two interaction sites in the oxDNA model.

**Large Deformation Behavior.** A harmonic restraint  $U = 1/2 k(d - d_0)^2$  of spring constant  $k = 0.4$  kcal mol<sup>-1</sup> Å<sup>-2</sup> was applied to the distance  $d$  between the centers of mass of the two arms to restrain the hinge fluctuations around a target distance  $d_0$ . By performing 150 ns-long MD simulations at different values of  $d_0$ , we were able to generate differently bent configurations of the hinges, well beyond the bending angles exhibited by the hinge at equilibrium. Each simulation also yielded average hinge bending angle  $\Phi$  and the average spring and joint end-to-end distances  $d_{\text{joint}}$  and  $d_{\text{spring}}$  associated with that angle.

**Force-Deformation Curves.** The force-deformation behavior of the ssDNA springs were investigated by applying an equal and opposite force to their two ends (terminal beads representing the two end phosphate groups in the oxDNA model) along their end-to-end vector (see Figure 8a, bottom). The force–extension curve was obtained by averaging the end-to-end distance measured over a 100 ns-long MD simulation at different applied forces. Similarly, the force-deformation behavior of the springless hinge was investigated by applying inward-pointing forces to the ends of the dsDNA helices at locations where they were connected to springs in the original hinge. The hinge bending angle was averaged over 100 ns-long MD simulations at each combination of forces applied to the three lower and upper layers of dsDNA helices (see Figure 8a, top).

**Simulation Codes and Data.** Files related to oxDNA simulations of the DNA hinges are provided at <https://github.com/gauravarya77/DNA-hinge-simulations>. These include: caDNAno design files of the hinges; Python scripts for converting caDNAno designs into initial oxDNA models and for substituting stretched bonds with harmonic restraints to generate relaxed configurations of the hinges; input option files for carrying out the relaxation procedure and the MD simulations; input topology and configuration files for the five hinges; and movie showing 100- $\mu$ s-long dynamics of a 0b hinge captured from an MD simulation.

## ASSOCIATED CONTENT

### Supporting Information

The Supporting Information is available free of charge on the ACS Publications website at DOI: 10.1021/acsnano.7b00242.

Comparison of simulated and experimentally obtained hinge angle distributions; Prediction of equilibrium hinge angles by CanDo; Joint and spring configurations in 0b hinges; Root mean square fluctuations of the entire hinge and of its two arms; H-bond occupancy results for 0b, 32b, and 74b hinges; Base-stacking distances for DNA helices comprising the hinge joints; Cross-correlations between different principal components; Differences in conformation of long and short springs; Total hinge potential energy and its electrostatic component; caDNAno hinge designs; Comparison of hinge angle distribution at two different salt concentrations; Hinge angle autocorrelations (PDF)

## AUTHOR INFORMATION

### Corresponding Author

\*E-mail: [garya@ucsd.edu](mailto:garya@ucsd.edu). Phone: +1 (858) 822-5542. Fax: +1 (858) 534-9553.

### ORCID

Carlos E. Castro: 0000-0001-7023-6105

Gaurav Arya: 0000-0002-5615-0521

### Notes

The authors declare no competing financial interest. Additional supporting research data related to oxDNA simulations of the DNA hinges for this article may be accessed at <https://github.com/gauravarya77/DNA-hinge-simulations>.

## ACKNOWLEDGMENTS

The authors thank Lifeng Zhou for providing the hinge designs, and Chaitanya Murthy and Dario Meluzzi for discussions. Computational resources were provided by the Extreme Science and Engineering Discovery Environment (XSEDE) Program, which is supported by the National Science Foundation Grant ACI-1053575.

## REFERENCES

- (1) Rothmund, P. W. K. Folding DNA to Create Nanoscale Shapes and Patterns. *Nature* **2006**, *440*, 297–302.
- (2) Liu, D.; Park, S. H.; Reif, J. H.; LaBean, T. H. DNA Nanotubes Self-Assembled from Triple-crossover Tiles as Templates for Conductive Nanowires. *Proc. Natl. Acad. Sci. U. S. A.* **2004**, *101*, 717–722.
- (3) Joshi, H.; Dwaraknath, A.; Maiti, P. K. Structure, Stability and Elasticity of DNA Nanotubes. *Phys. Chem. Chem. Phys.* **2014**, *17*, 1424–1434.
- (4) Jungmann, R.; Scheible, M.; Kuzyk, A.; Pardatscher, G.; Castro, C. E.; Simmel, F. C. DNA Origami-Based Nanoribbons: Assembly, Length Distribution, and Twist. *Nanotechnology* **2011**, *22*, 275301.
- (5) Hernández-Ainsa, S.; Misiunas, K.; Thacker, V. V.; Hemmig, E. A.; Keyser, U. F. Voltage-Dependent Properties of DNA Origami Nanopores. *Nano Lett.* **2014**, *14*, 1270–1274.
- (6) Bui, H.; Onodera, C.; Kidwell, C.; Tan, Y.; Graugnard, E.; Kuang, W.; Lee, J.; Knowlton, W. B.; Yurke, B.; Hughes, W. L. Programmable Periodicity of Quantum Dot Arrays with DNA Origami Nanotubes. *Nano Lett.* **2010**, *10*, 3367–3372.
- (7) Ding, B.; Deng, Z.; Yan, H.; Cabrini, S.; Zuckermann, R. N.; Bokor, J. Gold Nanoparticle Self-similar Chain Structure Organized by DNA Origami. *J. Am. Chem. Soc.* **2010**, *132*, 3248–3249.
- (8) Sun, W.; Boulais, E.; Hakobyan, Y.; Wang, W. L.; Guan, A.; Bathe, M.; Yin, P. Casting Inorganic Structures with DNA Molds. *Science* **2014**, *346*, 1258361.
- (9) Zadegan, R. M.; Jepsen, M. D. E.; Thomsen, K. E.; Okholm, A. H.; Schaffert, D. H.; Andersen, E. S.; Birkedal, V.; Kjems, J. Construction of a 4 Zeptoliters Switchable 3D DNA Box Origami. *ACS Nano* **2012**, *6*, 10050–10053.
- (10) Douglas, S. M.; Bachelet, I.; Church, G. M. A Logic-Gated Nanorobot for Targeted Transport of Molecular Payloads. *Science* **2012**, *335*, 831–834.
- (11) Douglas, S. M.; Marblestone, A. H.; Teerapittayanon, S.; Vazquez, A.; Church, G. M.; Shih, W. M. Rapid Prototyping of 3D DNA-origami Shapes with caDNAno. *Nucleic Acids Res.* **2009**, *37*, 5001–5006.
- (12) Williams, S.; Lund, K.; Lin, C.; Wonka, P.; Lindsay, S.; Yan, H. Tiamat: A Three-Dimensional Editing Tool for Complex DNA Structures. *Lect. Notes Comput. Sci.* **2009**, *5347*, 90–101.
- (13) Castro, C. E.; Kilchherr, F.; Kim, D.-N.; Shiao, E. L.; Wauer, T.; Wortmann, P.; Bathe, M.; Dietz, H. A Primer to Scaffolded DNA Origami. *Nat. Methods* **2011**, *8*, 221–229.
- (14) Kim, D.-N.; Kilchherr, F.; Dietz, H.; Bathe, M. Quantitative Prediction of 3D Solution Shape and Flexibility of Nucleic Acid Nanostructures. *Nucleic Acids Res.* **2012**, *40*, 2862–2868.
- (15) Veneziano, R.; Ratanalert, S.; Zhang, K.; Zhang, F.; Yan, H.; Chiu, W.; Bathe, M. Designer Nanoscale DNA Assemblies Programmed from the Top Down. *Science* **2016**, *352*, 1534.
- (16) Liedl, T.; Högberg, B.; Tytell, J.; Ingber, D. E.; Shih, W. M. Self-Assembly of Three-Dimensional Prestressed Tenegrity Structures from DNA. *Nat. Nanotechnol.* **2010**, *5*, 520–524.
- (17) Marras, A. E.; Zhou, L.; Su, H.-J.; Castro, C. E. Programmable Motion of DNA Origami Mechanisms. *Proc. Natl. Acad. Sci. U. S. A.* **2015**, *112*, 713–718.
- (18) Zhou, L.; Marras, A. E.; Su, H. J.; Castro, C. E. DNA Origami Compliant Nanostructures with Tunable Mechanical Properties. *ACS Nano* **2014**, *8*, 27–34.
- (19) Zhou, L.; Marras, A. E.; Su, H.-J.; Castro, C. E. Direct Design of an Energy Landscape with Bistable DNA Origami Mechanisms. *Nano Lett.* **2015**, *15*, 1815–1821.
- (20) SantaLucia, J.; Hicks, D. The Thermodynamics of DNA Structural Motifs. *Annu. Rev. Biophys. Biomol. Struct.* **2004**, *33*, 415–440.
- (21) Shih, W. M.; Quispe, J. D.; Joyce, G. F. A 1.7-kilobase Single-stranded DNA that Folds into a Nanoscale Octahedron. *Nature* **2004**, *427*, 618–621.
- (22) Copp, S. M.; Schultz, D. E.; Swasey, S.; Gwinn, E. G. Atomically Precise Arrays of Fluorescent Silver Clusters: A Modular Approach for Metal Cluster Photonics on DNA Nanostructures. *ACS Nano* **2015**, *9*, 2303–2310.
- (23) Birac, J. J.; Sherman, W. B.; Kopatsch, J.; Constantinou, P. E.; Seeman, N. C. Architecture with Gideon, a Program for Design in Structural DNA Nanotechnology. *J. Mol. Graphics Modell.* **2006**, *25*, 470–480.
- (24) Pan, K.; Kim, D.-N.; Zhang, F.; Adendorff, M. R.; Yan, H.; Bathe, M. Lattice-Free Prediction of Three-Dimensional Structure of Programmed DNA Assemblies. *Nat. Commun.* **2014**, *5*, 5578.
- (25) Sedeh, R. S.; Pan, K.; Adendorff, M. R.; Hallatschek, O.; Bathe, K.-J.; Bathe, M. Computing Nonequilibrium Conformational Dynamics of Structured Nucleic Acid Assemblies. *J. Chem. Theory Comput.* **2015**, *12*, 261–273.
- (26) Yoo, J.; Aksimentiev, A. *In Situ* Structure and Dynamics of DNA Origami Determined Through Molecular Dynamics Simulations. *Proc. Natl. Acad. Sci. U. S. A.* **2013**, *110*, 20099–20104.
- (27) Maingi, V.; Lelimosin, M.; Howorka, S.; Sansom, M. S. Gating-like Motions and Wall Porosity in a DNA Nanopore Scaffold Revealed by Molecular Simulations. *ACS Nano* **2015**, *9*, 11209–11217.
- (28) Li, C.-Y.; Hemmig, E. A.; Kong, J.; Yoo, J.; Hernández-Ainsa, S.; Keyser, U. F.; Aksimentiev, A. Ionic Conductivity, Structural Deformation, and Programmable Anisotropy of DNA Origami in Electric Field. *ACS Nano* **2015**, *9*, 1420–1433.
- (29) Joshi, H.; Kaushik, A.; Seeman, N. C.; Maiti, P. K. Nanoscale Structure and Elasticity of Pillared DNA Nanotubes. *ACS Nano* **2016**, *10*, 7780–7791.
- (30) Slone, S. M.; Li, C.-Y.; Yoo, J.; Aksimentiev, A. Molecular Mechanics of DNA Bricks: In Situ Structure, Mechanical Properties and Ionic Conductivity. *New J. Phys.* **2016**, *18*, 055012.
- (31) Iacovelli, F.; Falconi, M.; Knudsen, B. R.; Desideri, A. Comparative Simulative Analysis of Single and Double Stranded Truncated Octahedral DNA Nanocages. *RSC Adv.* **2016**, *6*, 35160–35166.
- (32) Potoyan, D. A.; Savelyev, A.; Papoian, G. A. Recent Successes in Coarse-Grained Modeling of DNA. *Wiley Interdiscip. Rev. Comput. Mol. Sci.* **2013**, *3*, 69–83.
- (33) Ouldrige, T. E.; Louis, A. A.; Doye, J. P. K. Structural, Mechanical, and Thermodynamic Properties of a Coarse-Grained DNA Model. *J. Chem. Phys.* **2011**, *134*, 085101.
- (34) Ouldrige, T. E.; Hoare, R. L.; Louis, A. A.; Doye, J. P. K.; Bath, J.; Turberfield, A. J. Optimizing DNA Nanotechnology Through Coarse-Grained Modeling: A Two-footed DNA Walker. *ACS Nano* **2013**, *7*, 2479–2490.
- (35) Šulc, P.; Ouldrige, T. E.; Romano, F.; Doye, J. P. K.; Louis, A. A. Simulating a Burnt-bridges DNA Motor with a Coarse-Grained DNA Model. *Nat. Comput.* **2014**, *13*, 535–547.
- (36) Romano, F.; Hudson, A.; Doye, J. P. K.; Ouldrige, T. E.; Louis, A. A. The Effect of Topology on the Structure and Free Energy Landscape of DNA Kissing Complexes. *J. Chem. Phys.* **2012**, *136*, 215102.
- (37) Matek, C.; Ouldrige, T. E.; Levy, A.; Doye, J. P. K.; Louis, A. A. DNA Cruciform Arms Nucleate through a Correlated but Asynchronous Cooperative Mechanism. *J. Phys. Chem. B* **2012**, *116*, 11616–11625.
- (38) Srinivas, N.; Ouldrige, T. E.; Sulc, P.; Schaeffer, J. M.; Yurke, B.; Louis, A. A.; Doye, J. P. K.; Winfree, E. On the Biophysics and Kinetics of Toehold-mediated DNA Strand Displacement. *Nucleic Acids Res.* **2013**, *41*, 10641–10658.

- (39) Rovigatti, L.; Bomboi, F.; Sciortino, F. Accurate Phase Diagram of Tetravalent DNA Nanostars. *J. Chem. Phys.* **2014**, *140*, 154903.
- (40) Matek, C.; Ouldrige, T. E.; Doye, J. P. K.; Louis, A. A.; Wang, X.; Llopis, P. M.; Rudner, D. Z.; Zhang, Y.; McEwen, A. E.; Crothers, D. M.; Levene, S. D.; Vijayan, V.; Zuzow, R.; O'Shea, E. K.; Strick, T. R.; Allemand, J. F.; Bensimon, D.; Bensimon, A.; Croquette, V.; Fye, R.; et al. Plectoneme Tip Bubbles: Coupled Denaturation and Writhing in Supercoiled DNA. *Sci. Rep.* **2015**, *5*, 7655.
- (41) Schreck, J. S.; Ouldrige, T. E.; Romano, F.; Šulc, P.; Shaw, L. P.; Louis, A. A.; Doye, J. P. DNA Hairpins Destabilize Duplexes Primarily by Promoting Melting Rather than by Inhibiting Hybridization. *Nucleic Acids Res.* **2015**, *43*, 6181–6190.
- (42) Doye, J. P. K.; Ouldrige, T. E.; Louis, A. a.; Romano, F.; Šulc, P.; Matek, C.; Snodin, B. E. K.; Rovigatti, L.; Schreck, J. S.; Harrison, R. M.; Smith, W. P. J. Coarse-Graining DNA for Simulations of DNA Nanotechnology. *Phys. Chem. Chem. Phys.* **2013**, *15*, 20395–414.
- (43) Ouldrige, T. E. DNA Nanotechnology: Understanding and Optimisation Through Simulation. *Mol. Phys.* **2015**, *113*, 1–15.
- (44) Snodin, B. E. K.; Romano, F.; Rovigatti, L.; Ouldrige, T. E.; Louis, A. A.; Doye, J. P. *ACS Nano* **2016**, *10*, 1724–1737.
- (45) Pettersen, E. F.; Goddard, T. D.; Huang, C. C.; Couch, G. S.; Greenblatt, D. M.; Meng, E. C.; Ferrin, T. E. UCSF Chimera-A Visualization System for Exploratory Research and Analysis. *J. Comput. Chem.* **2004**, *25*, 1605–1612.
- (46) Harrison, R. M.; Romano, F.; Ouldrige, T. E.; Louis, A. A.; Doye, J. P. K. Coarse-Grained Modelling of Strong DNA Bending I: Thermodynamics and Comparison to an Experimental “Molecular Vice”. *arXiv Preprint arXiv1506.09008* **2015**.
- (47) Olson, W. K.; Zhurkin, V. B. Working the Kinks out of Nucleosomal DNA. *Curr. Opin. Struct. Biol.* **2011**, *21*, 348–357.
- (48) Asanuma, H.; Liang, X.; Nishioka, H.; Matsunaga, D.; Liu, M.; Komiyama, M. Synthesis of Azobenzene-Tethered DNA for Reversible Photo-regulation of DNA Functions: Hybridization and Transcription. *Nat. Protoc.* **2007**, *2*, 203–212.
- (49) Abendroth, J. M.; Bushuyev, O. S.; Weiss, P. S.; Barrett, C. J. Controlling Motion at the Nanoscale: Rise of the Molecular Machines. *ACS Nano* **2015**, *9*, 7746–7768.
- (50) Snodin, B. E.; Randisi, F.; Mosayebi, M.; Šulc, P.; Schreck, J. S.; Romano, F.; Ouldrige, T. E.; Tsukanov, R.; Nir, E.; Louis, A. A.; Doye, J. P. K. Introducing Improved Structural Properties and Salt Dependence into a Coarse-Grained Model of DNA. *J. Chem. Phys.* **2015**, *142*, 234901.
- (51) Agrawal, V.; Arya, G.; Oswald, J. Simultaneous Iterative Boltzmann Inversion for Coarse-Graining of Polyurea. *Macromolecules* **2014**, *47*, 3378–3389.
- (52) Lukacs, G. L.; Haggie, P.; Seksek, O.; Lechardeur, D.; Freedman, N.; Verkman, A. S. Size-Dependent DNA Mobility in Cytoplasm and Nucleus. *J. Biol. Chem.* **2000**, *275*, 1625–1629.
- (53) Grant, B. J.; Rodrigues, A. P. C.; ElSawy, K. M.; McCammon, J. A.; Caves, L. S. D. Bio3d: An R Package for the Comparative Analysis of Protein Structures. *Bioinformatics* **2006**, *22*, 2695–2696.